Optical and Physicochemical Properties of Silica-Supported TiO$_2$ Photocatalysts

Javier Marugán and Rafael Van Grieken

Dept. of Chemical and Environmental Technology, Universidad Rey Juan Carlos,
C/ Tulipán s/n 28933 Móstoles (Madrid), Spain

Orlando M. Alfano and Alberto E. Cassano

Instituto de Desarrollo Tecnológico para la Industria Química (INTEC), Universidad Nacional del Litoral-CONICET,
Güemes 3450, (3000) Santa Fe, Argentina

Commercial applications of photocatalysis in slurry reactors employing titanium dioxide particles present the disadvantage of the additional cost associated with the downstream catalyst separation. In past years a significant effort has been made to develop supported titania photocatalysts on particles of larger size in order to facilitate the sedimentation recovery process. In this work, two different silica materials have been used for preparing immobilized catalysts. Their physicochemical characteristics have been compared with those corresponding to two commercially available unsupported titanium dioxide catalysts. However, for reaction kinetics and reactor design purposes, three additional properties must be known: (i) the spectral specific radiation absorption coefficient, (ii) the spectral specific radiation scattering coefficient, and (iii) the asymmetry factor of a model for the angular distribution of the scattered photons (the phase function). They have been determined with specially designed spectrophotometer transmission, diffuse transmittance, and diffuse reflectance experiments and constitute the most significant addition to this contribution. © 2006 American Institute of Chemical Engineers AIChE J, 52: 2832–2843, 2006
Keywords: photoreactor, photocatalyst, supported TiO$_2$, absorption, scattering

Introduction

TiO$_2$ photocatalysis has been shown as an environmental-friendly technology for the detoxification of highly toxic and non-biodegradable pollutants commonly present in air and domestic or industrial wastewaters. Many authors have reported a large number of chemical pollutants susceptible to being oxidized through heterogeneous photocatalysis.[1-5] These processes are based on the use of UV radiation to activate a semiconductor material, usually titanium dioxide, on whose surface the oxidation

of the pollutant is carried out. As TiO$_2$ is usually a non-porous solid, to maximize photoactivity particles should be small enough to offer a high specific surface area. Unfortunately for applications in aqueous phase, such a small particle size means high separation costs to remove the catalyst once the reaction is finished. Consequently, the commercial applications of these technologies for the treatment of aqueous effluents are limited by both the recovery of the catalyst after the reaction and the economic feasibility of the photocatalytic processes, conditioned by the efficiency in the use of the employed radiation. On these bases, many efforts have been devoted to the development of supported photocatalysts with suitable recovery properties.[6,7]

Despite the large number of supported TiO$_2$ photocatalysts reported in the past years, no attempts have been made to

determine the optical parameters (absorption and scattering coefficients and phase function) of aqueous suspensions of this kind of composite materials. These values are required for the evaluation of the radiation absorbed by the catalyst suspension in order to quantify, for example, the absolute quantum yields of the photocatalytic reaction. The optical properties are also needed for the rigorous design and scaling-up of the photocatalytic reactors to solve the radiation transfer equation (RTE).[8] This solution provides the distribution of light intensities in the reaction space, required to calculate the radiation activation step of the kinetic model that will be incorporated in the reactor mass balance.

Taking into account that radiation emission can be neglected at the low operating temperatures of the photocatalytic processes, the RTE takes the following expression:

$$\frac{dI_{\lambda,\Omega}(\underline{x}, t)}{ds} = -\underbrace{\kappa_\lambda(x, t)I_{\lambda,\Omega}(x, t)}_{\text{ABSORPTION}} - \underbrace{\sigma_\lambda(\underline{x}, t)I_{\lambda,\Omega}(\underline{x}, t)}_{\text{OUT-SCATTERING}}$$
$$+ \underbrace{\frac{\sigma_\lambda(\underline{x}, t)}{4\pi} \int_{\Omega'=4\pi} p(\underline{\Omega}' \to \underline{\Omega})I_{\lambda,\Omega'}(\underline{x}, t)d\Omega'}_{\text{IN-SCATTERING}} \quad (1)$$

The solution of this equation permits the evaluation of the radiation field at any point inside the reactor space. Once the intensities are known, the incident radiation can be readily obtained according to:

$$G_\lambda(\underline{x}, t) = \int_{\Omega=4\pi} I_{\lambda,\underline{\Omega}}(\underline{x}, t)d\Omega \quad (2)$$

And the radiation absorption rate is:

$$e_\lambda^a(\underline{x}, t) = \kappa_\lambda(\underline{x}, t)G_\lambda(\underline{x}, t) \quad (3)$$

Integrating Eq. 3 in the whole polychromatic wavelength range leads to the local volumetric rate of photon absorption (LVRPA) at any point of the reactor:

$$LVRPA = e^a(\underline{x}, t) = \int_{\lambda_1}^{\lambda_2} \int_{\Omega=4\pi} \kappa_\lambda(\underline{x}, t)I_{\lambda\underline{\Omega}}(\underline{x}, t)d\Omega d\lambda \quad (4)$$

As can be seen from Eq. 1, the values of the optical properties of the catalyst suspensions inside the photocatalytic reactor are unmistakably required for the description of the radiation field and the evaluation of the photon absorption rate. The present work deals with the evaluation of the absorption and scattering coefficients and the asymmetry factor of a model of the phase function of several silica-supported TiO$_2$ photocatalysts recently developed.[9,10] Experimental and theoretical modifications from previously reported procedures[11,12] have been required in order to quantify the optical properties of these materials. The influence of the titanium dioxide loading and the type of silica support is studied. Differences with the optical properties of unsupported TiO$_2$ and their consequences for the photoreactor design are also analyzed.

Synthesis and Characterization of the Supported Photocatalyst

Two different silica materials were used as supports for the preparation of immobilized TiO$_2$ photocatalysts. The first one was an amorphous SiO$_2$ commercially available (INEOS Silica ES70Y). Its wide pore size distribution is in contrast to the textural properties of the second silica support, the so-called SBA-15, a mesostructured material with a very well defined pore size in the range of the mesopores. The latter was prepared in our laboratory according to the original method of Zhao et al.[13]

Incorporation of titania into the supports was carried out employing a sol-gel method. Hydrolysis of titanium tetraisopropoxide and condensation inside the porous structure of the silica was followed by hydrothermal treatment for TiO$_2$ crystallization. A detailed explanation of the synthesis procedure can be found elsewhere.[9,14] Depending of the silica support, the catalysts will be named as x%TiO$_2$/SiO$_2$ or x%TiO$_2$/SBA-15 (where x represents the nominal wt% of titania loading).

For comparison purposes, two different commercial titanium dioxide samples, Aldrich and Degussa P25, have been used. Both materials are well-known photocatalysts with an activity widely reported in the literature.

Chemical analyses for determining the exact titanium content of the supported photocatalysts were performed using a Varian VISTA AX inductively coupled plasma atomic emission spectrophotometer (ICP-AES). Samples were dissolved with fluorhydric acid, and quantification was carried out by using the emission line at 336.112 nm after calibration with certified standards.

The measured TiO$_2$ content of the different materials is reported in Table 1. The deviations from the nominal content incorporated to the synthesis procedure of the supported photocatalysts are lower than 7%.

Scanning electron microscopy (SEM) micrographs were taken on a JEOL JSM-6400 working at an acceleration voltage of 15-30 kV. Energy dispersive X-ray microanalysis (EDX) was carried out with the microprobe attached to the microscope in order to determine the homogeneity in the titanium dioxide distribution over the support. Micrographs of these materials have been previously reported for Aldrich and Degussa titanium dioxide[11] and for the silica supports and the supported photocatalysts.[10] From these contributions, the commercial TiO$_2$ materials consist of very small primary particles of sizes usually smaller than 1 μm. The amorphous silica consists in discrete spherical particles of 10-50 μm in diameter. The incorporation of TiO$_2$ into the support scarcely modifies the particle size of the material and produces a reduced generation of smaller particles by mechanical breakage of the support during the synthesis stage.[14] Concerning the SBA-15 silica, it consists of large rope-like domains of bean-shaped primary particles approximately 1 μm in diameter, aggregated into wheat-like macrostructures.[10,13] In this case, the incorporation of titania into the support does not modify the primary particles, but reduces the particle size of the secondary agglomerates.

Nevertheless, the particles sizes determined by microscopy do not represent the size of the aggregates formed in the aqueous suspensions of the solids, due to the formation of flocks.[11] In order to assess the particle agglomerate diameters,

Table 1. Physical Properties of the Studied Materials

	Degussa P25 TiO$_2$	Aldrich TiO$_2$	SiO$_2$ Support	20% TiO$_2$/SiO$_2$	40% TiO$_2$/SiO$_2$	60% TiO$_2$/SiO$_2$	SBA-15 SiO$_2$	20% TiO$_2$/SBA-15
TiO$_2$ content								
%TiO$_2$ (wt%)	100	100	—	21.4	37.9	58.9	—	19.3
Average aggregate size								
D$_{AGGREGATE}$ (μm)	0.7[11]	0.3[11]	15.4	16.4	20.6	25.3	27.3	18.6
Specific surface area								
S$_{BET}$ (m^2 g^{-1})	52.0	7.14	257.4	251.2	242.7	222.7	640.0	532.0
Pore volume								
V$_{PORE}$ (cm^3 g^{-1})	—	—	1.15	1.06	0.92	0.70	0.96	0.78
Average pore size								
D$_{PORE}$ (nm)	—	—	17.9	17.0	15.1	12.6	6.3	6.0
TiO$_2$ Crystal size (XRD)	31 (anat.)							
D$_{CRYSTAL}^{XRD}$ (nm)	54 (rut.)	1800	—	6.9	7.2	8.0	—	6.2
Band gap								
E$_g$ (eV)	3.70	3.44	—	3.70	3.68	3.58	—	3.83

a focused beam reflectance measurement system FBRM M500LF manufactured by LASENTEC (USA.) was used. The FBRM instrument operates by scanning a highly focused laser beam at a fixed speed across particles in suspension. Measuring the time duration of the backscattered light from these particles renders a characteristic measurement of the particle geometry. More details of the application of this technique in flocculation processes can be found elsewhere.[15]

Suspensions of the different materials were prepared by dispersing 1 g of the solids in 1 liter of distillate water. Measurements were carried out after 60 min of homogenization by magnetic stirring. Figure 1 shows the particle size distribution determined for every one of the silica based materials. As can be observed, the SBA-15 silica and the 20%TiO$_2$/SBA-15 photocatalyst present wide distributions of sizes. It is worth noting that the incorporation of titania into the support produces a decrease in the average size of the aggregate material. This fact could be explained by the mechanical fracture of the SBA-15 secondary particles produced during the synthesis of the supported photocatalysts.

Regarding the amorphous silica based photocatalysts, an opposite behavior is observed, increasing the average aggregate size as the titania content increases. In this case, as the discrete silica particles of the support are not agglomerated, it seems that the incorporation of TiO$_2$ into the support facilitates the formation of aggregates in aqueous suspensions. This is probably caused by the modification of the surface charge of the particles due to the presence of titania on the external surface of the silica.

Table 1 reports the average particle size calculated for every material in comparison with the values previously reported by Cabrera et al.[11] for titanium dioxide commercial samples. These results are considered much more related to the optical behavior of the catalyst suspensions than the values determined by microscopy.

The BET surface areas and pore volumes of the samples were calculated from the nitrogen adsorption–desorption isotherms at 77K obtained in a Micromeritics Tristar 3000 equipment. For the determination of the pore size distributions, the BJH model was used assuming a cylindrical geometry of the pores.

The calculated textural properties are summarized in Table 1. The incorporation of titania into the amorphous silica support produces a progressive decrease of the specific surface area, pore volume, and average pore size of the material as the titanium dioxide loading increases. However, the decrease in the pore volume is more significant than that of the specific surface area. As titanium dioxide particles usually are non porous, these results suggest that the supported materials present a high titania surface area due to the formation of very small titania particles. More details about the adsorption isotherms of these materials can be found elsewhere.[9]
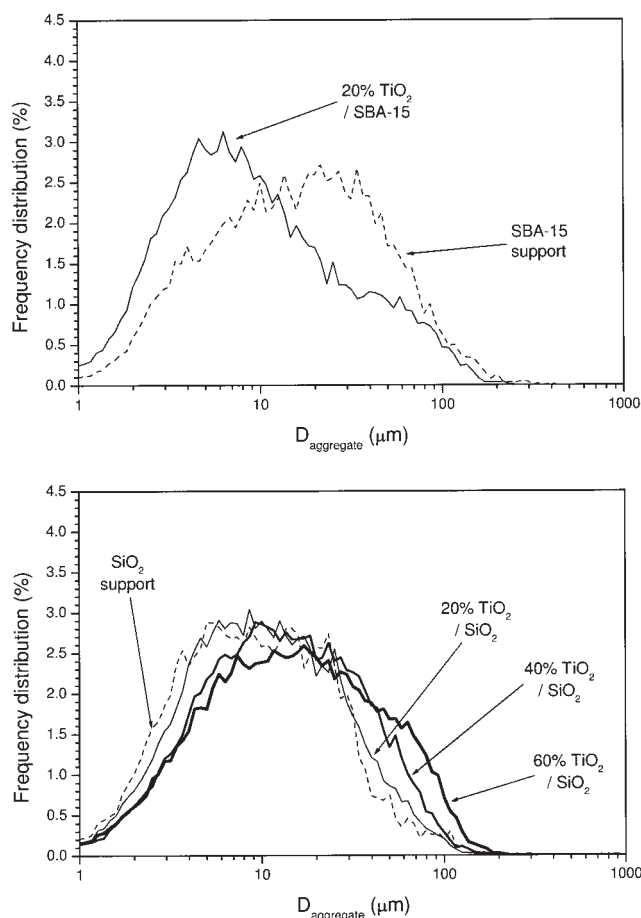

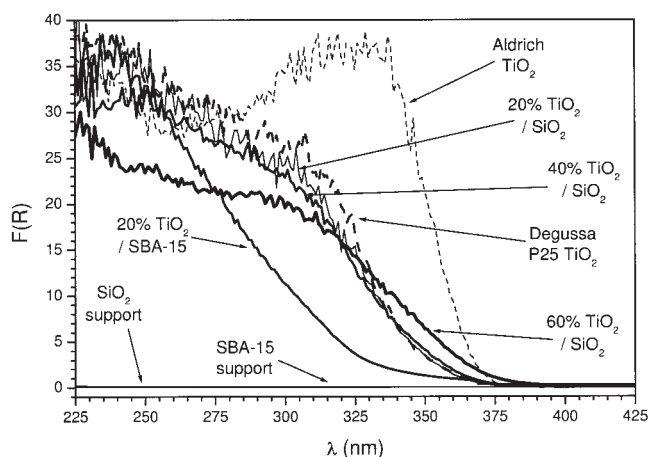**Figure 1. Particle size distribution of the solid suspensions.**

Figure 2. Diffuse reflectance spectra of the different materials.

Powder X-ray diffraction (XRD) patterns were collected on a Philips X'PERT MPD diffractometer using monochromatic Cu K_α radiation and scanning 2θ from 20 to 70° with a step size of 0.02°. The step time was 2 s, adequate to obtain a good signal-to-noise ratio in the main diffractions of the two studied TiO_2 crystalline phases, (1 0 1) anatase ($2\theta \sim 25.3°$) and (1 1 0) rutile ($2\theta \sim 27.4°$).

The X-ray diffraction patterns of the supported photocatalysts evidence that in all the samples only the anatase crystalline phase is present. Despite the large collecting time, the wide peaks and the low signal to noise ratio confirm that the average crystals size of the TiO_2 clusters is very low. These sizes have been estimated by the Scherrer equation using the calcite (1 0 4) diffraction signal ($2\theta \sim 29.4°$) as internal standard to calculate the instrumental width (0.15°). The results are also shown in Table 1. There is a small increase in the crystal size as the loading increases, although all materials present average values below 10 nm, which means that quantum size effects must be taken into account. Additional information can be found elsewhere.[9]

Concerning the commercial TiO_2 materials, important differences are found between Aldrich and Degussa samples. The former consist of well crystallized pure anatase, whereas the latter show a 4:1 anatase to rutile ratio. In this case, the crystal sizes estimated by the broadening of the main diffraction signals are 31 nm and 54 nm for anatase and rutile, respectively.

Diffuse reflectance spectra in the 200-500 nm range were recorded with a Varian Cary 500 Scan UV–VIS–NIR spectrophotometer equipped with an integrating sphere diffuse reflectance accessory, using polytetrafluoroethylene as reference scatterer. The reflectance data were reported as the Kubelka–Munk function, F(R), whose value could be assumed to be proportional to the absorption.[16]

Figure 2 shows the diffuse reflectance spectra of the studied materials. First of all, it is important to notice that the silica support is totally transparent in the wavelength of interest, confirming the feasibility of using the whole porous structure of this material as support for TiO_2 semiconductor crystals.

Concerning the supported photocatalysts, all of them show the typical shape of the titanium dioxide materials, but with a shift to more energetic wavelengths when compared with the bulk anatase phase.

The extrapolation of the linear part of the $(F(R) \cdot h\nu)^2$ versus $h\nu$ plots leads to the value of the band gap value of these materials.[17] The calculated E_g values are also included in Table 1. As can be seen, a decrease in the band gap energy is observed when increasing the TiO_2 content supported on the amorphous silica. These results have been previously observed and related to crystal growth as titania loading is increased.[9] Regarding the 20%TiO_2/SBA-15, a much higher value of E_g is obtained, probably due to the controlled particle size achieved by the use of the SBA-15 silica as support.[10]

Summarizing the results presented in Table 1, the supported photocatalysts show larger average particle sizes and smaller titanium dioxide crystals in comparison with powder TiO_2. Additionally, it is important to remark that as the titania loading increases, a slight increase in the titania crystal size is observed that produces an small decrease in the optical band gap value.

Extinction Coefficients

According to the radiation transport theory,[18,19] the sum of the absorption coefficient and the scattering coefficient is called the *extinction coefficient* ($\beta_\lambda = \kappa_\lambda + \sigma_\lambda$). For a heterogeneous medium in which both phenomena take place simultaneously, this coefficient can be obtained from the conventional spectrophotometric transmittance measurements.[11] The most accurate values are obtained when minimizing the scattering-in and none of the scattered-out radiation is collected by the detector.

Extinctance measurements were made for: (i) each of the four supported photocatalysts and both supports, (ii) four different concentrations of every material suspended in distilled water and stirred for 60 min, and (iii) 13 different wavelengths (from 285 to 405 nm in equally separated intervals of 10 nm).

The experimental setup used for the determination of the extinction coefficients has been modified from previous work in order to optimize the measurements for the supported photocatalysts suspensions. First, the thickness of the optical cell is higher than that used for titanium dioxide suspensions due to the much lower optical density of the supported materials (10 mm instead of 1-5 mm for unsupported titanium dioxide[11,12]). Second, as was previously reported, the immobilized photocatalysts show higher settling rates,[14] hindering the measurements of the suspensions extinctances in static conditions. Consequently, a flow-cell based system (Figure 3) has been developed in order to overcome this problem. A reservoir with the catalysts suspended in water is magnetically stirred while a peristaltic pump continuously drives the suspension to the flow-cell in the spectrophotometer and back to the reservoir. In this way, the obtained measurements were absolutely independent of time, that is, under steady state conditions.

The spectrophotometer was an Optronic OL series 750 interfaced with a data station. In order to reduce the out-scattered radiation entering the detector chamber, a narrow vertical slit (20 mm high × 1.5 mm wide) was placed in the center of the detector view angle. This slit coincides exactly with the radiation beam coming out of an empty sample cell. The baseline of the instrument for the whole wavelength was adjusted by using distilled water. For each suspension, the wavelength range was swept from 285 to 405 nm. Three repetitions every
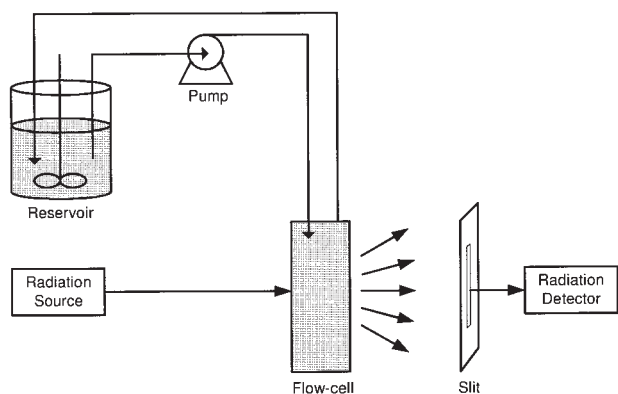
Figure 3. Experimental setup for measurement of the suspension transmittance.

5 min were carried out to confirm that the measured data do not vary with time.

The napierian volumetric extinction coefficient (β_λ) is calculated from the experimental values at each wavelength (obtained in the spectrophotometer as transmittance readings, T_λ) as follows:

$$\beta_\lambda \text{ (cm}^{-1}) = \frac{-\ln(T_\lambda)}{L \text{ (cm)}} \tag{5}$$

where L represents the cell path length (1 cm).

Over the investigated range of concentrations, the plot of β_λ versus the mass catalyst concentration (C_{mp}) provided a straight line through the origin. The specific extinction coefficient [$\beta_\lambda^* = \beta_\lambda/C_{mp}$ (cm^2 g^{-1})] can be obtained by application of a standard linear regression on the data with forced intercept at the origin.

Figure 4 shows the values of the specific extinction coefficients as a function of wavelength for the studied materials. The value of β_λ^* of both silica supports is almost independent of the wavelength, as could be expected for a pure scattering material (no absorption has been detected for this material, see Figure 2). Nevertheless, there are significant differences between both supports, with extinction coefficients almost four times higher for the SBA-15. This fact is probably related to the different texture of the aggregates of this silica material as compared with the amorphous silica.

Concerning the supported photocatalysts, all of them present similar trends in which the extinction coefficient slightly decreases at higher wavelengths where absorption becomes negligible according to the spectra displayed in Figure 2. In all cases, the values are higher than that from the corresponding support. For the materials supported on amorphous silica, the extinction coefficients increase with the titania loading from 20 wt% to 40 wt%, but similar results to the latter are obtained for the 60 wt% material. They reach values that approximately double the ones of the silica support. Similarly, the 20%TiO₂/SBA-15 presents extinction coefficients twice those shown by SBA-15.

Consequently, the increase in the titania content leads to higher extinction coefficients for the whole range of studied wavelength range. This result is independent of the relative increase or decrease of the average aggregates size in comparison with the silica support, as can be observed from the data

shown in Table 1. The characterization of the silica-supported photocatalysts has shown that incorporation of titania into the particles of the support is achieved[10]; this means that a material with higher titania percentage consists of fewer silica particles supporting more semiconductor crystals per particle. From this assumption, it can be suggested that a lower scattering of radiation could be expected. Consequently, the increase in the extinction coefficients as the wavelength is decreased must probably be explained as a result of the absorption contribution to the extinction coefficient.

Finally, it is worth noticing that in all cases the specific extinction coefficients estimated for all the silica-based material suspensions are much lower (approximately ten times) than those reported for powder titanium dioxide materials.[11] For instance, the values of β_λ^* at 335 nm for the catalysts 20%TiO₂/SiO₂, 40%TiO₂/SiO₂, 60%TiO₂/SiO₂, and 20%TiO₂/SBA-15 are 1541.5, 1910.2, 1915.9, and 7730.2 cm²g^{-1}, respectively, whereas values of 68,000 and 37,000 cm²g^{-1} are obtained for Degussa P25 and Aldrich TiO₂.[11]

One of the reasons for these differences is the higher aggregates size observed for the silica-based materials in comparison with both TiO₂ samples (see Table 1). If we consider that the scattering contribution to the radiation extinction is to some extent always related to the average aggregates size, significant differences in the σ^* values should be expected from the distributions depicted in Figure 1. Nevertheless, the scattering phenomenon is probably not enough to account for such large variations, and significant disparities in the absorption coefficients must certainly be expected.

Evaluation of the Absorption Coefficient and the Asymmetry Factor

An independent measurement is required for the evaluation of the absorption coefficient. Once known, the scattering coefficient can be obtained by subtraction from the extinction coefficient. As was shown by Cabrera et al.,[11] these additional experiments could consist of spectrophotometric measurements carefully designed to collect all the radiation forwardly scattered by the sample by means of an integrating sphere (see
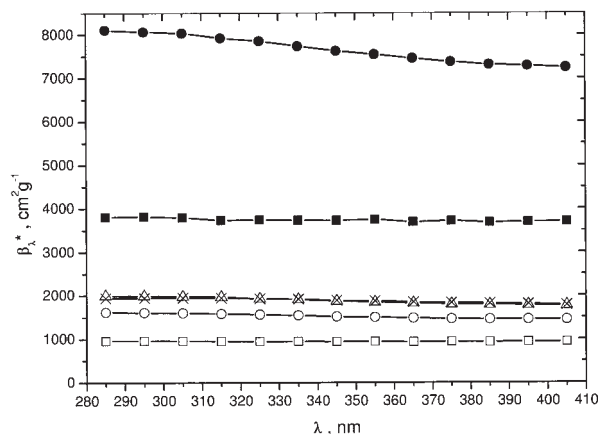

Figure 4. Specific extinction coefficient of different materials as a function of wavelength.

Key: (□) silica; (○) 20%TiO₂/SiO₂; (△) 40%TiO₂/SiO₂; (×) 60%TiO₂/SiO₂; (■) SBA-15; and (●) 20%TiO₂/SBA-15. Numerical values of β_λ^* are shown in Appendix A, Table A1.
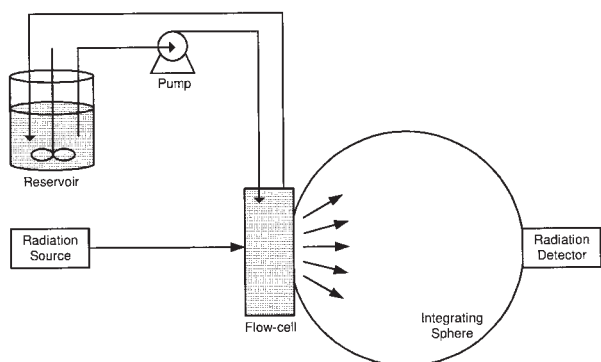
Figure 5. Experimental setup for measurement of the diffuse transmittance.

Figure 5). The radiation reaching the detector accounts for two types of contributions: (i) transmitted radiation and (ii) forwardly scattered radiation. Notice that radiation scattered backward and through both sides of the cell is lost and not accounted for by the detector; consequently, the absorption coefficient cannot be directly calculated from these measurements.

On the other hand, Satuf et al.[12] have recently reported that reflectance measurements could also be carried out in order to obtain, simultaneously with the absorption coefficient, the angular distribution of scattered radiation (the phase function). With this procedure the adoption of a given phase function is not required; this procedure results in an improvement of the method initially proposed by Cabrera et al.[11] The reflectance measurements were made according to the scheme represented in Figure 6. The radiation beam enters the integrating sphere with a direction that is neither pointed to the sample cell nor to the detector. In this way, the radiation backscattered from the suspension is incorporated to the photons collected by the detector.

Diffuse transmittance (DT_λ) and diffuse reflectance (DR_λ) measurements were made for: (i) each of the four supported photocatalysts and both supports, (ii) four different concentrations of every material suspended in distilled water and stirred for 60 min, and (iii) 13 different wavelengths (from 285 to 405 nm in equally separated intervals of 10 nm). Samples were prepared exactly in the same way as described for the extinctance measurements.

An OL 740–80 integrating sphere reflectance attachment was used together with the spectrophotometer for both measurements. The PTFE (polytetrafluoroethylene) integrating sphere coating permits the operation in the whole wavelength range of interest. PTFE has also been used as scattering reference in the comparison port of the integrating sphere attachment and as sample for the calibration of the system. For each suspension, the wavelength range was swept from 285 to 405 nm. Three repetitions every 5 min were carried out to confirm that the measured data do not vary with time. The diffuse reflectance values were corrected to discount the influence of the reflection in both cell glass walls.

Analysis of the Experimental Data

To calculate the values of the specific absorption and scattering coefficients, these experimental systems have to be mod-

eled and the RTE must be solved. First of all, the mathematical model developed by Satuf et al.[12] for the analysis of the optical properties of powder TiO_2 suspensions was applied. However, that model led to inconsistent results, such as high absorption coefficients for the silica materials, in contrast with the DR-UV/Vis spectra displayed in Figure 2. The reason was that the hypothesis assumed for the development of the symmetry and boundary conditions of this model was not achieved in the case of the supported photocatalysts suspensions. That means that a 1-dimensional, 1-directional model cannot be applied.

This conclusion is supported by the fact that the sum of the experimental values of diffuse transmittance and diffuse reflectance at the same λ accounts for less than 70% of the radiation even at high wavelengths in which the spectra shown in Figure 2 stated that the materials do not absorb. According to the described experimental setup, this phenomenon could be explained only by the existence of an important amount of radiation being scattered-out through the lateral sides of the spectrophotometric cell. The reasons of this difference between supported and powder photocatalysts are mainly two: first, the extinction coefficients of the powder TiO_2 suspensions are much higher, and second, but directly related, the cell path is much larger for the supported photocatalysts, resulting in an increase in the side to front dimensions ratio. Consequently, a rectangular 2-dimensional, 2-directional model has been developed in order to analyze the experimental data.

Preserving the spherical coordinate system for radiation propagation, the RTE in bidimensional Cartesian coordinates takes the following expression:

$$\mu \frac{\partial I_{\lambda\Omega}(x, y)}{\partial x} + \eta \frac{\partial I_{\lambda\Omega}(x, y)}{\partial y} = -(\kappa_\lambda + \sigma_\lambda)I_{\lambda\Omega}(x, y)$$

$$+ \frac{\sigma_\lambda}{4\pi} \int_{\Omega'=4\pi} p(\Omega' \rightarrow \Omega)I_{\lambda\Omega'}(x, y)d\Omega' \quad (6)$$

To obtain the radiation field, an expression for the phase function is required. The Henyey-Greenstein's phase function seems to be a good choice. This function presents the advantage that with only one adjustable parameter it is able to reproduce very different scattering radiation distributions. It is expressed as follows:
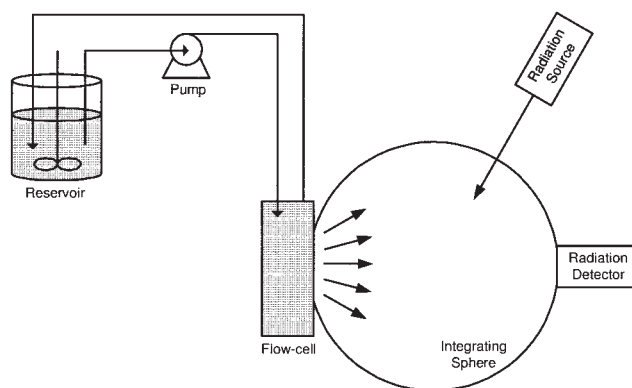

Figure 6. Experimental setup for measurement of the diffuse reflectance.
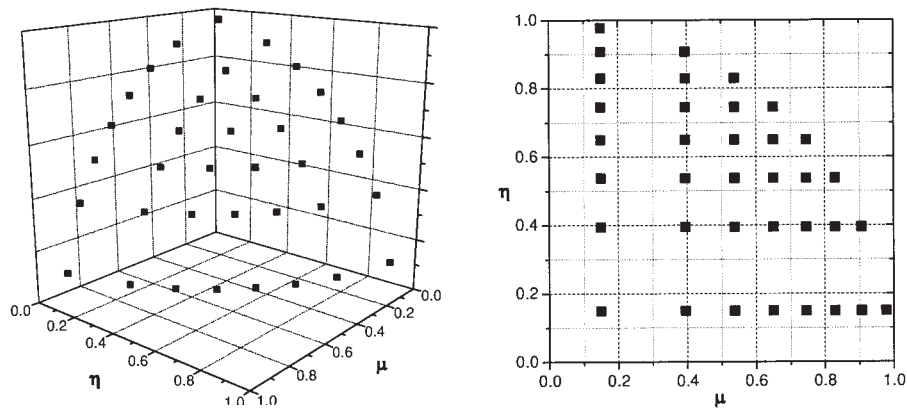
Figure 7. Spatial mesh and quadrant definition for the 2-dimensional, 2-directional discretization of the spectrophotometric cell.

$$p(\underline{\Omega} \cdot \underline{\Omega}') = p(\cos \alpha) = \frac{1 - g^2}{(1 + g^2 - 2g \cos \alpha)^{3/2}} \quad (7)$$

where g is the asymmetry factor of the scattered radiation distribution. A value of zero for g represents an isotropic phase function in which all directions contributions are equally distributed. Positive values for g mean that the scattering is produced preferably in the forward direction, and negative values indicate preeminence of the backward direction. A detailed explanation of the use of this function to represent the scattering produced by the photocatalyst suspensions can be found in the work of Satuf et al.[12]

To solve the RTE a special numerical method developed in the area of neutron transport theory has been applied. The validity of this procedure, called the *discrete ordinate method* (DOM), has been widely shown in the literature.[20,21] The DOM transforms the integro-differential RTE into a system of finite differences algebraic equations that can be solved by machine computation.

Figure 7 displays the spatial and directional discretization

performed on the spectrophotometric cell. As shown by Duderstadt and Martin,[22] for multidimensional geometries it is advisable to derive the finite difference relations directly from the radiation balance for each mesh cell, rather than introducing the finite difference approximation directly into the RTE.

Assuming linear radiation profiles inside the cell, the cell-centered intensity could be calculated from the average of the cell-edged intensities according to the symmetric diamond difference relations:

$$I_m^{i,j} = \frac{1}{2}(I_m^{i+(1/2),j} + I_m^{i-(1/2),j}) \tag{8}$$

$$I_m^{i,j} = \frac{1}{2}(I_m^{i,j+(1/2)} + I_m^{i,j-(1/2)}) \tag{9}$$

These relations reduce the number of unknowns, leading to the following expression for the monochromatic radiation balance in the direction m inside the bidimensional cell i,j:

$$I_m^{i,j} = \frac{2\Delta y_j|\mu_m|}{D}I_m^{i\pm(1/2),j} + \frac{2\Delta x_i|\eta_m|}{D}I_m^{i,j\pm(1/2)} + \frac{S_m^{i,j}}{D} \tag{10}$$

where

$$D = 2\Delta y_j|\mu_m| + 2\Delta x_i|\eta_m| + \beta_\lambda \Delta x_i \Delta y_j \tag{11}$$

and the source term, corresponding to the in-scattering contribution, is given by:

$$S_m^{i,j} = \frac{\sigma_\lambda}{4\pi}\int_{4\pi} p(\Omega' \rightarrow \Omega_m)I_m^{i,j}d\Omega' \tag{12}$$

Equation 10 is relatively easy to solve in comparison with other bidimensional systems employing curvilinear coordinates in which "angular redistribution phenomena" must be taken into account.[21]

Figure 8 summarizes the algorithm developed for the calculation of the monochromatic radiation field inside the spectrophotometric cell. The progression through the spatial mesh is defined by the following boundary conditions:

(i) Known inlet radiation at x = 0 (quadrants II and III).

(ii) Transparent (non reflecting) walls, which means null inlet radiation at $x = L_x$ (quadrants I and IV), $y = 0$ (quadrants III and IV), and $y = L_y$ (quadrants I and II).

Consequently, computation of every quadrant begins from the cell corner in which both boundary conditions are known. First, the cell-centered intensity is calculated from the inlet values and, second, the outlet values for every direction are obtained from the diamond differences relations. Iteration of the computation is required until the intensities initially employed for the calculus of the source terms coincide with the properly calculated values.

To compare the model predictions with the experimental values, the results have been interpreted in terms of radiation fluxes. For our model, the fluxes in the forward direction (q^+) and in the backward direction (q^-) are:

$$\langle q_\lambda^+\rangle_y(x) = \left\langle \int_{\phi=0}^{\phi=\pi}\int_{\theta=0}^{\theta=\pi} I_{\lambda\Omega}(x,y)\cos\theta d\theta d\phi\right\rangle_y \tag{13}$$

$$\langle q_\lambda^-\rangle_y(x) = \left\langle \int_{\phi=\pi}^{\phi=2\pi}\int_{\theta=0}^{\theta=\pi} I_{\lambda\Omega}(x,y)\cos\theta d\theta d\phi\right\rangle_y \tag{14}$$

where the values of I_λ are obtained from the solution of the RTE (Eq. 6) for a given value of the two parameters: κ_λ and g.

The theoretical values of DT_λ and DR_λ are given by:

$$DT_\lambda = \frac{\langle q_\lambda^+\rangle_y(x=L)}{\langle q_\lambda^+\rangle_y(x=0)} \tag{15}$$

$$DR_\lambda = \frac{\langle q_\lambda^-\rangle_y(x=0)}{\langle q_\lambda^+\rangle_y(x=0)} \tag{16}$$

In this way, a Levenberg-Marquardt nonlinear multiparameter estimator algorithm can be used to estimate the best values of *specific* absorption coefficient ($\kappa_\lambda*$) and the asymmetry factor (g) that minimizes the errors between the experimental results and the model predictions for all the concentrations studied and for every material.

In order to assure the confidence of the results, further adjustments have been done in which independent values of the *volumetric* absorption coefficient (κ_λ) and g were calculated for every catalyst concentration experiment. For all the studied materials, the plot of κ_λ versus C_{mp} is a straight line that intercepts the origin, and very similar values of g are calculated for the four concentrations.

Concerning the dependence on wavelength of the asymmetry factor (g), the results do not show clear tendencies. In fact, due to the higher sensibility of both model responses with g, small variations on this parameter produce plots of $\kappa_\lambda*$ versus λ that are slightly sharper than those shown by Satuf et al.[12] for the unsupported TiO_2 materials, with much higher values of the absorption coefficient. Then, for the supported materials, it is preferably to assume a unique value for g, independent of the wavelength. This assumption is supported by the fact that the absorption and scattering coefficients are expected to show a much stronger dependence on λ. Consequently, the best values for the parameters have been obtained through a quasi-Newton optimization algorithm implemented to calculate the value of g that minimizes the error of the predictions for all wavelengths. For each iteration of the optimization procedure, a Levenberg-Marquardt algorithm is applied to each wavelength to estimate the value of the specific absorption coefficient.

Figures 9 and 10 show the values of the specific absorption and scattering coefficients ($\sigma_\lambda = \beta_\lambda - \kappa_\lambda$) as a function of wavelength calculated for the studied materials, whereas Table 2 summarizes the values for g. As can be expected, it is worth mentioning that the results obtained for the absorption coefficients are null for both silica supports in the whole studied wavelength range. This means that all the radiation extinction observed for these materials is produced by scattering. These results are in agreement with the diffuse reflectance spectra displayed in Figure 2 and, furthermore, they validate the 2-di-
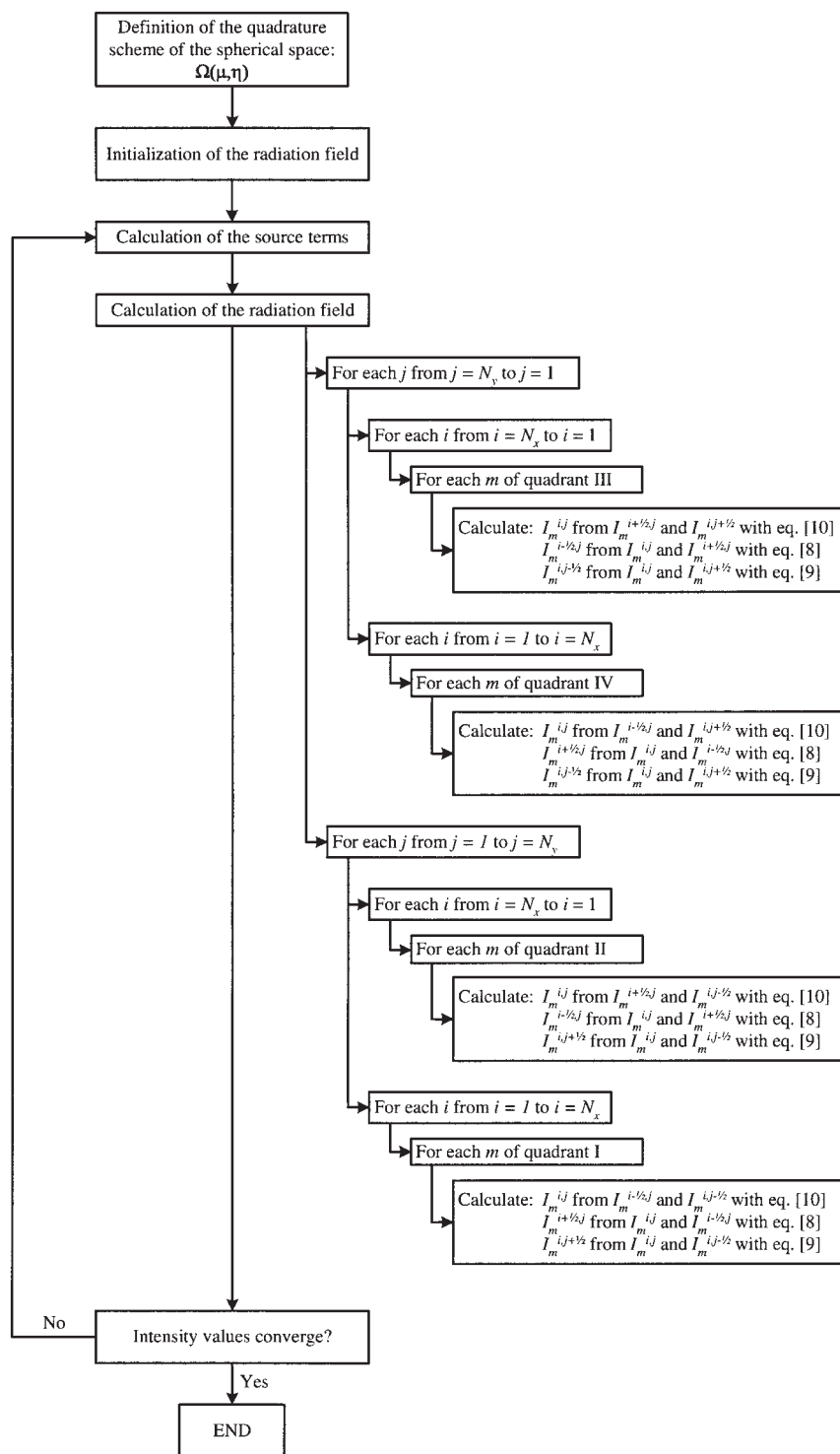
Definition of the quadrature scheme of the spherical space: $\Omega(\mu,\eta)$

↓

Initialization of the radiation field

↓

Calculation of the source terms

↓

Calculation of the radiation field

For each j from $j = N_y$ to $j = 1$

For each i from $i = N_x$ to $i = 1$

For each m of quadrant III

Calculate: $I_m^{i,j}$ from $I_m^{i+\frac{1}{2},j}$ and $I_m^{i,j+\frac{1}{2}}$ with eq. [10]
$I_m^{i-\frac{1}{2},j}$ from $I_m^{i,j}$ and $I_m^{i+\frac{1}{2},j}$ with eq. [8]
$I_m^{i,j-\frac{1}{2}}$ from $I_m^{i,j}$ and $I_m^{i,j+\frac{1}{2}}$ with eq. [9]

For each i from $i = 1$ to $i = N_x$

For each m of quadrant IV

Calculate: $I_m^{i,j}$ from $I_m^{i-\frac{1}{2},j}$ and $I_m^{i,j+\frac{1}{2}}$ with eq. [10]
$I_m^{i+\frac{1}{2},j}$ from $I_m^{i,j}$ and $I_m^{i-\frac{1}{2},j}$ with eq. [8]
$I_m^{i,j-\frac{1}{2}}$ from $I_m^{i,j}$ and $I_m^{i,j+\frac{1}{2}}$ with eq. [9]

For each j from $j = 1$ to $j = N_y$

For each i from $i = N_x$ to $i = 1$

For each m of quadrant II

Calculate: $I_m^{i,j}$ from $I_m^{i+\frac{1}{2},j}$ and $I_m^{i,j-\frac{1}{2}}$ with eq. [10]
$I_m^{i-\frac{1}{2},j}$ from $I_m^{i,j}$ and $I_m^{i+\frac{1}{2},j}$ with eq. [8]
$I_m^{i,j+\frac{1}{2}}$ from $I_m^{i,j}$ and $I_m^{i,j-\frac{1}{2}}$ with eq. [9]

For each i from $i = 1$ to $i = N_x$

For each m of quadrant I

Calculate: $I_m^{i,j}$ from $I_m^{i-\frac{1}{2},j}$ and $I_m^{i,j-\frac{1}{2}}$ with eq. [10]
$I_m^{i+\frac{1}{2},j}$ from $I_m^{i,j}$ and $I_m^{i-\frac{1}{2},j}$ with eq. [8]
$I_m^{i,j+\frac{1}{2}}$ from $I_m^{i,j}$ and $I_m^{i,j-\frac{1}{2}}$ with eq. [9]

↓

Intensity values converge? — No (loop back to Calculation of the source terms)

↓ Yes

END

Figure 8. Algorithm developed for the resolution of the RTE using the DOM.

mensional, 2-directional model of the photon balance in the spectrophotometer cell. Regarding the phase function, the value of 0.866 obtained for the parameter g indicates that the radiation scattering is mainly directed to forward directions. Similar values of g are calculated for the rest of the materials.

Concerning the silica supported photocatalysts, in all cases null absorption coefficients are obtained for wavelengths above 385 nm. In contrast, below this threshold wavelength, an important increase of the κ_λ^* values is observed, especially for the 20%TiO$_2$/SBA-15 photocatalysts. These results are in agreement with the optical behavior expected from the diffuse reflectance spectra shown in Figure 2. However, whereas the conclusions extracted from the solid DR-UV/Vis measurements are exclusively qualitative, the quantitative determina-
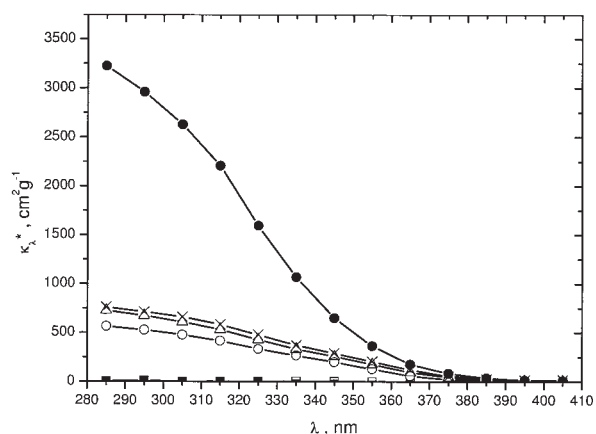
Figure 9. Specific absorption coefficient of different materials as a function of wavelength.

Key: ($\square$) silica; ($\bigcirc$) 20%TiO$_2$/SiO$_2$; ($\triangle$) 40%TiO$_2$/SiO$_2$; ($\times$) 60%TiO$_2$/SiO$_2$; ($\blacksquare$) SBA-15; and ($\bullet$) 20%TiO$_2$/SBA-15. Numerical values of κ_λ^* are shown in Appendix A, Table A2.

tion of the absorption and scattering coefficients allows the design and simulation of a photocatalytic reactor.

As regards the influence of the TiO$_2$ loading, apparently little differences are observed among the absorption and scattering coefficients of the 20%TiO$_2$/SiO$_2$, 40%TiO$_2$/SiO$_2$, and 60%TiO$_2$/SiO$_2$ catalysts. However, a deeper analysis of these results must be done, as the reported values are *specific coefficients*, that is, per gram of solid material. Consequently, if we assume that the silica content does not produce absorption, it could be concluded that the 60%TiO$_2$/SiO$_2$ material shows similar κ_λ^* and σ_λ^* values as the 40%TiO$_2$/SiO$_2$ material with a third less titania.

From the agglomerate size distributions shown in Figure 1 it could probably be expected that the increase in the TiO$_2$ content should produce a decrease in the scattering coefficient, as the average particle size is slightly higher. Additionally, an important increase in the absorption coefficient could be expected due to the higher semiconductor content, the active
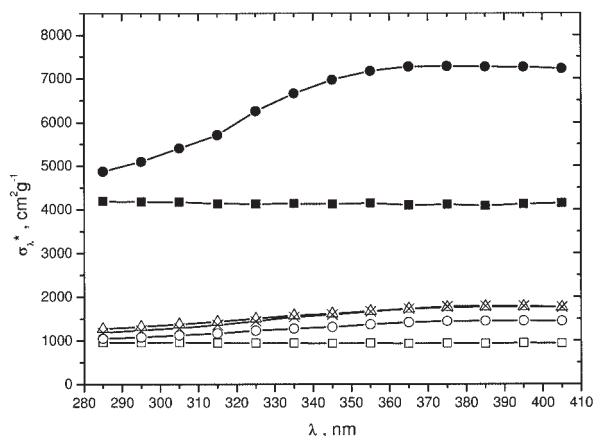

Figure 10. Specific scattering coefficient of different materials as a function of wavelength.

Key: ($\square$) silica; ($\bigcirc$) 20%TiO$_2$/SiO$_2$; ($\triangle$) 40%TiO$_2$/SiO$_2$; ($\times$) 60%TiO$_2$/SiO$_2$; ($\blacksquare$) SBA-15; and ($\bullet$) 20%TiO$_2$/SBA-15. Numerical values of σ_λ^* are shown in Appendix A, Table A3.

Table 2. Asymmetry Factor of the Henyey-Greenstein Phase Function for the Different Materials

	g
SiO$_2$ support	0.866
20% TiO$_2$/SiO$_2$	0.815
40% TiO$_2$/SiO$_2$	0.803
60% TiO$_2$/SiO$_2$	0.745
SBA-15	0.862
20% TiO$_2$/SBA-15	0.877

material for photon absorption. However, the results show that the incorporation of titania leads to a little increase in the values of σ_λ^*, despite the lower number of particles in the suspension. On the other side, the increase in the values of κ_λ^* is not so drastic as could have been expected, which probably means that the titania loading in the silica particles is so high that screening effects of the TiO$_2$ crystal located on the most external positions of the silica particles are taking place.

Finally, it must be pointed out that, in comparison with the results presented by Satuf et al.[12] for different commercial TiO$_2$ materials, the values observed in Figure 9 for the absorption coefficients of the silica supported photocatalyst are much lower. For instance, the values of κ_λ^* at 335 nm for the 20%TiO$_2$/SiO$_2$, 40%TiO$_2$/SiO$_2$, 60%TiO$_2$/SiO$_2$, and 20%TiO$_2$/SBA-15 catalysts are 268.8, 333.3, 372.3, and 1067.6 cm^{2}g^{-1}, respectively, whereas values of 28,000 and 17,000 are obtained for Degussa P25 and Aldrich TiO$_2$.[12] Furthermore, it is remarkable that not only the absolute values of the absorption coefficients are lower, but also in relative terms. Whereas 40% of the extinction produced by the pure titania suspensions is due to the absorption contribution, less than 20% of the extinction observed in the silica-supported photocatalysts suspensions is produced by photon absorption (more than 80% of the radiation is scattered).

Conclusions

Physical and chemical properties of silica-supported titanium dioxide catalysts have been measured. Of particular relevance for possible applications is the complete characterization of the optical properties of the particle suspensions as a function of wavelength. These optical properties are: the specific absorption and scattering coefficients and the dimensionless asymmetry factor representing the phase function.

The employed method was based on extinctance and diffuse reflectance and transmittance spectrophotometric measurements of titanium dioxide supported on silica suspensions, the solution of the radiative transfer equation in the sample cell, and the application of a nonlinear multiparameter regression procedure to adjust theoretical values to experimental data.

All reported values show differences between the several types of prepared supported material; these differences are more pronounced when the comparison is made with respect to the unsupported materials. The most prominent contrast is observed in the data of the radiation absorption coefficient and the ratio of the absorption to the extinction values.

These results are very important in designing applications because they necessarily imply a significant change in the optical thickness of the reaction medium that directly affects the geometry and dimensions of a practical reactor. Also, the development and optical characterization of these supported titania photocatalysts on large size particles will facilitate the

sedimentation recovery process and, consequently, the commercial applications of photocatalysis in slurry reactors.

Notation

C_{mp} = catalyst mass concentration, g m^{-3}
DT = spectrophotometric diffuse transmittance measurement, dimensionless
DR = spectrophotometric diffuse reflectance measurement, dimensionless
e^a = volumetric rate of photon absorption, Einstein m^{-3} s^{-1}
G = incident radiation from all directions, Einstein m^{-2} s^{-1}
I = radiation intensity, Einstein m^{-2} s^{-1} sr^{-1}
L = cell optical path, m
T = spectrophotometric transmittance measurement, dimensionless
p = phase function, dimensionless
q = radiative flux, Einstein m^{-2} s^{-1}
s = linear coordinate along the direction of radiation propagation Ω, m
S = source term of the RTE, Einstein m^{-3} s^{-1} sr^{-1}
t = time, s
$\underline{x}$ = vector representing position in a 3D space, m
x,y = rectangular Cartesian coordinates, m

Greek letters

β = napierian volumetric extinction coefficient, m^{-1}
β^* = napierian specific extinction coefficient, m^2 g^{-1}
θ = spherical coordinate, rad
ϕ = spherical coordinate, rad
η = director cosine to y axis, dimensionless
κ = napierian volumetric absorption coefficient, m^{-1}
κ^* = napierian specific absorption coefficient, m^2 g^{-1}
λ = wavelength, nm
μ = director cosine to x axis, dimensionless
σ = napierian volumetric scattering coefficient, m^{-1}
σ^* = napierian specific scattering coefficient, m^2 g^{-1}
Ω = solid angle of radiation propagation about the direction Ω, sr
$\underline{\Omega}$ = unit vector in the direction of radiation propagation

Subscripts

λ = indicates a dependence on wavelength
0 = indicates inlet condition

Superscripts

$+$ = indicates forward direction
$-$ = indicates backward direction

Special symbols

$-$ = indicates a vectorial quantity
$\langle\ \rangle$ = indicates average value

Literature Cited

1. Ollis DF, Al-Ekabi H., Eds. *Photocatalytic Purification and Treatment of Water and Air*. Amsterdam: Elsevier; 1993.
2. Fox MA, Dulay M. Heterogeneous photocatalysis. *Chem Rev*. 1993; 93:341-357.
3. Blake D. Bibliography of Work on the Photocatalytic Removal of Hazardous Compounds from Water and Air, NREL, Golden, CO; May 1994. Available on the web at http://www.nrel.gov. (1st update: October 1994; 2nd update: October 1996; 3rd update: January 1999; 4th update: October 2001.)
4. Hoffmann MR, Martin ST, Choi W, Bahnemann DW. Environmental applications of semiconductor photocatalysis. *Chem Rev*. 1995;95:69-96.
5. Herrmann JM. Heterogeneous photocatalysis: fundamentals and applications to the removal of various types of aqueous pollutants. *Catal Today*. 1999;53:115-129.
6. Pozzo RL, Baltanás MA, Cassano AE. Supported titanium oxide as photocatalyst in water decontamination: state of the art. *Catal Today*. 1997;39:219-231.
7. Byrne JA, Eggins BR, Brown NMD, McKinney B, Rouse M. Immobilisation of TiO$_2$ powder for the treatment of polluted water. *Applied Catal B: Environmental*. 1998;17:25-36.
8. Cassano AE, Martín CA, Brandi RJ, Alfano OM. Photoreactor analysis and design: fundamentals and applications. *Industrial Eng Chem Res*. 1995;34:2155-2201.
9. van Grieken R, Aguado J, López-Muñoz MJ, Marugán J. Synthesis of size-controlled silica-supported TiO$_2$ photocatalysts. *J Photochem Photobiol A: Chem*. 2002;148:315-322.
10. López Muñoz MJ, van Grieken R, Aguado J, Marugán J. Role of the support on the activity of silica-supported TiO$_2$ photocatalysts. *Catal Today*. 2005;101:307-314.
11. Cabrera MI, Alfano OM, Cassano AE. Absorption and scattering coefficients of titanium dioxide particulate suspensions in water. *J Phys Chem*. 1996;100:20043-20050.
12. Satuf ML, Brandi RJ, Cassano AE, Alfano OM. An experimental method to evaluate the optical properties of aqueous titanium dioxide suspensions. *Industrial Eng Chem Res*. 2005;44:6643-6649.
13. Zhao D, Feng J, Huo Q, Melosh N, Fredickson GH, Chmelka BF, Stucky GD. Triblock copolymer syntheses of mesoporous silica with periodic 50 to 300 angstrom pores. *Science*. 1998;279:548-552.
14. Aguado J, van Grieken R, López-Muñoz MJ, Marugán J. Removal of cyanides in wastewater by supported TiO$_2$-based photocatalysts. *Catal Today*. 2002;75:95-102.
15. Blanco A, Fuente E, Negro C, Tijero J. Flocculation monitoring: focused beam reflectance measurements as a measurement tool. *Canadian J Chem Eng*. 2002;80:734-740.
16. Anderson C, Bard AJ. Improved photocatalytic activity and characterization of mixed TiO$_2$/SiO$_2$ and TiO$_2$/Al$_2$O$_3$. *J Phys Chem*. 1997; 101:2611-2616.
17. Lassaleta G, Fernandez A, Espinos JP, Gonzalez-Elipe AR. Spectroscopic characterization of quantum-sized TiO$_2$ supported on silica: influence of size and TiO$_2$-SiO$_2$ interface composition. *J Phys Chem*. 1995;99:1484-1490.
18. Ozisik MN. *Radiative Transfer and Interactions with Conduction and Convection*. New York: Wiley; 1973.
19. Siegel R, Howell JR. *Thermal Radiation Heat Transfer* (3rd ed.). Washington, DC: Hemisphere; 1992.
20. Alfano OM, Negro AC, Cabrera MI, Cassano AE. Scattering effects produced by inert particles in photochemical reactors. 1. Model and experimental verification. *Industrial Eng Chem Res*. 1995;34:488-499.
21. Romero LR, Alfano OM, Cassano AE, Cylindrical photocatalytic reactors. Radiation absorption and scattering effects produced by suspended fine particles in an annular space. *Industrial Eng Chem Res*. 1997;36:3094-3109.
22. Duderstadt JJ, Martin WR. *Transport Theory*. New York: Wiley; 1979.

Appendix: Numerical Values of the Optical Properties

Table A1. Specific Extinction Coefficient (β_λ^*, cm^2 s^{-1}) of the Different Materials

λ (nm)	SiO$_2$ Support	20% TiO$_2$/SiO$_2$	40% TiO$_2$/SiO$_2$	60% TiO$_2$/SiO$_2$	SBA-15	20% TiO$_2$/SBA-15
285	962.1	1617.4	1997.7	1944.2	3809.8	8105.1
295	960.4	1609.3	1992.9	1950.3	3814.3	8058.9
305	955.4	1601.5	1983.8	1947.1	3791.6	8030.9
315	949.3	1578.7	1966.7	1943.5	3730.2	7915.3
325	943.8	1561.3	1931.6	1923.4	3741.4	7852.1
335	945.6	1541.5	1910.2	1915.9	3730.6	7730.2
345	940.9	1515.7	1873.8	1885.0	3726.2	7623.5
355	941.5	1497.9	1847.4	1871.6	3747.7	7538.6
365	933.5	1478.5	1818.0	1848.9	3688.9	7449.1
375	937.8	1461.7	1799.7	1832.3	3716.6	7367.0
385	929.0	1453.6	1786.9	1814.6	3677.3	7306.4
395	937.3	1451.0	1779.2	1806.8	3691.8	7278.9
405	937.1	1446.9	1764.6	1783.0	3704.2	7240.5

Table A2. Specific Absorption Coefficient (κ_λ^*, cm^2 s^{-1}) of the Different Materials

λ (nm)	SiO$_2$ Support	20% TiO$_2$/SiO$_2$	40% TiO$_2$/SiO$_2$	60% TiO$_2$/SiO$_2$	SBA-15	20% TiO$_2$/SBA-15
285	1.9	565.0	726.4	760.2	5.8	3223.7
295	4.5	528.1	673.0	711.5	9.1	2959.6
305	1.4	477.1	608.7	661.6	0.5	2627.0
315	2.0	415.7	531.8	583.2	0	2206.2
325	1.3	335.3	429.4	479.0	0	1594.7
335	4.9	268.8	333.3	372.3	0	1067.6
345	4.0	200.8	257.9	290.4	0	651.1
355	2.3	129.3	178.5	206.2	0	365.6
365	0.8	58.6	95.8	121.5	0	176.9
375	3.3	20.3	42.7	55.5	0	85.8
385	0	5.9	17.4	24.9	0	37.0
395	0	0.7	7.6	16.7	0	17.2
405	0.2	1.1	6.6	18.7	0	8.5

Table A3. Specific Scattering Coefficient (σ_λ^*, cm^2 s^{-1}) of the Different Materials

λ (nm)	SiO$_2$ Support	20% TiO$_2$/SiO$_2$	40% TiO$_2$/SiO$_2$	60% TiO$_2$/SiO$_2$	SBA-15	20% TiO$_2$/SBA-15
285	960.2	1052.4	1271.3	1184.0	4197.4	4881.4
295	956.0	1081.3	1319.9	1238.8	4181.6	5099.3
305	954.0	1124.4	1375.1	1285.5	4173.4	5403.9
315	947.3	1163.0	1434.9	1360.4	4138.8	5709.1
325	942.5	1226.0	1502.2	1444.4	4135.7	6257.4
335	940.7	1272.7	1576.9	1543.6	4138.1	6662.6
345	937.0	1315.0	1615.9	1594.6	4125.0	6972.4
355	939.2	1368.6	1669.0	1665.4	4150.4	7173.0
365	932.7	1419.9	1722.2	1727.4	4100.3	7272.2
375	934.5	1441.4	1757.0	1776.8	4118.5	7281.2
385	929.4	1447.7	1769.5	1789.7	4088.8	7269.4
395	938.9	1450.3	1771.6	1790.1	4126.2	7261.7
405	936.9	1445.8	1758.0	1764.3	4150.7	7232.1